Commun. Comput. Phys.
doi: 10.4208/cicp.OA-2020-0098

Vol. **x**, No. x, pp. 1-30
xxx 20xx

A Computational Model for Simulation of Shallow Water Waves by Elastic Deformations in the Topography

Alia Al-Ghosoun*, Ashraf S. Osman and Mohammed Seaid

Department of Engineering, University of Durham, South Road, Durham DH1 3LE, UK.

Received 26 May 2020; Accepted (in revised version) 2 November 2020

Abstract. We propose a coupled model to simulate shallow water waves induced by elastic deformations in the bed topography. The governing equations consist of the depth-averaged shallow water equations including friction terms for the water free-surface and the well-known second-order elastostatics formulation for the bed deformation. The perturbation on the free-surface is assumed to be caused by a sudden change in the bottom beds. At the interface between the water flow and the bed topography, transfer conditions are implemented. Here, the hydrostatic pressure and friction forces are considered for the elastostatic equations whereas bathymetric forces are accounted for in the shallow water equations. The focus in the present study is on the development of a simple and accurate representation of the interaction between water waves and bed deformations in order to simulate practical shallow water flows without relying on complex partial differential equations with free boundary conditions. The effects of location and magnitude of the deformation on the flow fields and free-surface waves are investigated in details. Numerical simulations are carried out for several test examples on shallow water waves induced by sudden changes in the bed. The proposed computational model has been found to be feasible and satisfactory.

AMS subject classifications: 74B10, 65M08, 35L53, 76B15, 74J40, 76B07

Key words: Shallow water equations, elastic deformation, sudden bed changes, finite element method, finite volume method, deformable beds.

1 Introduction

In this study the problem of shallow water flows under conditions of abrupt changes to the bathymetry is considered. The idea is to develop an accurate and efficient compu-

*Corresponding author. *Email addresses:* alia.r.al-ghosoun@durham.ac.uk (A. Al-Ghosoun), ashraf.osman@durham.ac.uk (A. S. Osman), m.seaid@durham.ac.uk (M. Seaid)

tational approach to simulate such flows which pose a great challenge due to the differences in temporal and spatial scales. The free-surface flow which is commonly modeled by the shallow water equations coupled with the sudden changes of bathymetry is investigated numerically. It has been observed in nature that free-surface flows can sometimes be triggered by an abrupt or a sudden change in the bathymetry [1]. A clear example is the tsunamis or landslides that pour into a water body in oceans or lakes. The common practice in modeling such free-surface flows is to assume that the displacement of the free-surface is the same as the displacement of the bed, and it happens concurrently due to incompressibility of the water. Thus, as an initial condition one applies a static source together with a translation of the seabed deformation onto the free-surface flow. Such an approach was first presented for the field of modeling tsunamis in [6] and referred to as *the passive approach* in [8]. The validity of such an approach was reported in [9] among others. The passive approach neglects the so-called rupture velocity and the rise time of the fault/bathymetry change dynamics. Investigations have been undertaken to understand the rupture velocity and rise time in many engineering applications. For example, the study in [24] took into account the rise time, and the rupture velocity has also been accounted for in [12]. In [21], work has been undertaken in which a numerical integration of the time-dependent elasticity equations as well as time-dependent fluid equations was considered. Over the past years, the development of efficient and increasingly accurate numerical models of nonlinear shallow water equations over variable beds has been a continuous challenge in coastal engineering communities see [7, 20, 30] among others. Since these models are considered to be theoretically challenging and practically important, researchers are currently working on developing efficient and accurate computational tools to model shallow water waves by elastic deformations in the topography. This represents a great challenge due to the time and space scales for which the abrupt changes took places versus the evolution of the water free-surface.

The commonly used finite difference schemes in the numerical solution of the nonlinear shallow water equations are non-conservative leading to volume loss and energy dissipation as the wave steepness increases and the flow approaches discontinuities [31]. Recent advances in seismic inverse algorithms enable accurate descriptions of the rise time and rupture propagation over the source area. Furthermore, this model provides a time series of the vertical displacement and velocity that constitute the bottom boundary condition of a non-hydrostatic model for transfer of kinetic and potential energies to the water. One limitation of this method is the appearance of oscillations in the computational results when applied to more complex geometries [27]. The depth-integrated method was reformulated, and hence a non-hydrostatic model was derived in the spherical coordinate system for basin-wide waves propagation [32]. However, this method suffers from a drawback in that it cannot guarantee the conservation of momentum in the numerical scheme. Each of the aforementioned numerical modeling techniques has its own features and drawbacks when it is applied to the shallow water system. The finite difference scheme is considered to be easy to implement. However, the scheme is not accurate when dealing with complex geometries such as the characterization of

the coastlines during the simulation [18]. To deal with these limitations, refined mesh approaches are applied to increase the resolution of certain areas of interest [34]. Nevertheless, there are still some problems facing this approach when the waves are reflected from the coastline outside the finer mesh as such waves are not well resolved.

Finite element methods are more flexible in modeling shallow water flows in a complex geometry as they can be formulated for a wide range of mesh topologies [29, 33, 35]. A limitation of the finite element method lies when the solution exhibits large gradients [5]. In addition, the finite element method also suffers from its inability to conserve mass and momentum during the simulations. The finite volume techniques are widely known by researchers for dealing with mobile beds, even though such techniques are also well suited for solving the partial differential equations that are included in shallow water flows. These methods have become standard in solving the free-surface flows and shock waves problems as they guarantee the conservation property during the simulation. The most significant problem facing the finite volume techniques when dealing with a mobile bed is the treatment of the geometric source terms, where the challenge is in the balancing between gradient and source terms when time variations are small. This problem is numerically non-trivial, and methods that are not well balanced would generate spurious oscillations in their results [26]. The transient generation of waves due to the coupling between the free-surface and sea floor has been considered by few authors only. Generally, there are some specific cases where the bottom deformation becomes a very important factor. Other studies relied on experimental techniques by lowering or raising a box at one end of the channel [17]. The purpose of this study is to develop a novel model for numerical simulation of shallow water waves by elastic deformations in the topography. Accounting for elastic deformations in the shallow water flows is new and a coupled set of partial differential equations is proposed in this work for their modeling.

In the current study, a coupled finite element/finite volume method for solving free-surface flow problems over deformable beds is proposed. The governing equations consist of the one-dimensional nonlinear shallow water equations for the water flow and a two-dimensional linear elasticity model for the bed deformation. Deformations in the topography can be caused by a localized force which causes propagations of water waves with different amplitudes and frequencies. Coupling conditions at the interface are also investigated in this study and a well-balanced finite volume method using non-uniform grids is implemented to avoid interpolation procedures at the interface between the finite element nodes and the finite volume cells. Frictional forces along with hydrodynamical forces are also accounted for in the water flow model. On the other hand a force is sampled from the hydrostatic pressure and applied on the bed surface during the time process. To the best of our knowledge, developing a coupled finite element/finite volume method for solving free-surface flow problems over deformable beds is presented for the first time. The paper is organized as follows. Description of the coupled model for shallow water waves induced by elastic deformations is presented in Section 2. Section 3 is devoted to the formulation of the numerical methods used for the solution procedure. We consider a two-dimensional finite element method for the bed deformations whereas

a well-balanced finite volume method is implemented for the free-surface waves. In Section 4, we present numerical results and examples for shallow water flows over elastic beds. Our new approach is shown to enjoy the expected accuracy as well as the efficiency. Concluding remarks are given in Section 5.

2 Shallow water waves by elastic deformation in beds

The physical model used in the present study consists of the well-known shallow water equations coupled with additional equations to describe the elastic deformation in the bed. The shallow water system has been widely used to model water flows under the influence of gravity and it uses the assumption that the vertical scale is much smaller than any typical horizontal scale. This class of equations can be derived by depth-averaging the incompressible Navier-Stokes equations subject to a hydrostatic pressure, see for example [11]. For one-dimensional problems, the equations read

$$\frac{\partial h}{\partial t}+\frac{\partial (hv)}{\partial x}=0, \tag{2.1a}$$

$$\frac{\partial (hv)}{\partial t}+\frac{\partial}{\partial x}\left(hv^2+\frac{1}{2}gh^2\right)=-gh\frac{\partial B}{\partial x}+\tau_f, \tag{2.1b}$$

where t is the time variable, x the space coordinate, $h(x,t)$ the water depth, $v(x,t)$ the water velocity, g the gravitational constant and B the bed topography. In (2.1), τ_f is the friction slope term which models the bottom friction effects using the Manning empirical form,with M_b being the Manning roughness coefficient at the bed, τ_f is defined by

$$\tau_f=-gM_b^2h\frac{v|v|}{h^{4/3}}. \tag{2.2}$$

It is well known that the system (2.1) is strictly hyperbolic with real and distinct eigenvalues given as

$$\lambda_1=v-\sqrt{gh}, \qquad \lambda_2=v+\sqrt{gh}. \tag{2.3}$$

Notice that Eps. (2.1) have to be solved in a time interval and spatial domain equipped with given boundary and initial conditions. In practice, these conditions are problem dependent and their discussion is postponed for Section 4 where numerical examples are discussed. In the shallow water equations (2.1), the function B corresponds to the topography layer characterizing the bed level. For fixed bottom topography, *i.e.* $B=B(x)$, Eps. (2.1) reduce to the standard shallow water equations. In the current work, we assume that a deformation takes place such that the bed level depends on the time variable as well. This requires an additional equation for its evolution and deformation. To motivate the discussion, we consider a simple example of bed deformation as depicted in Fig. 1. Similar techniques have been used to model elastic models of the earthquake cycle for a long strike-slip fault, see for instance [13, 19].

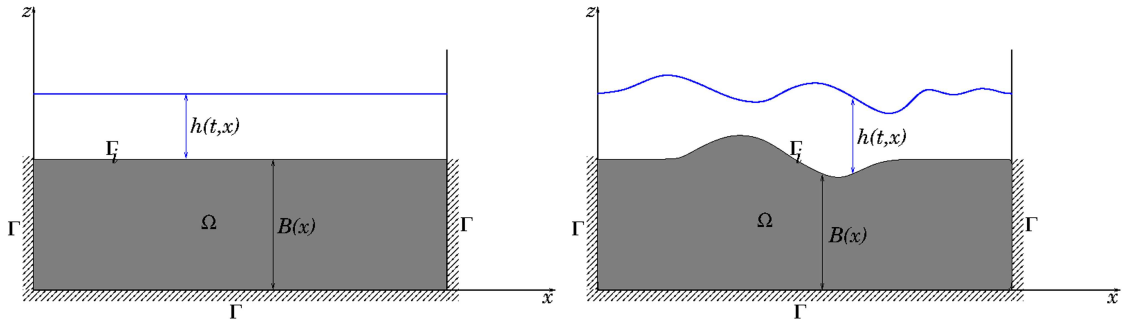

Figure 1: Coupled system before bed deformation (left plot) and after bed deformation (right plot).

In solid mechanics, the two-dimensional constitutive relations of an isotropic elastic bed in presence of body forces can be reformulated as [23]

$$\frac{\partial \sigma_x}{\partial x}+\frac{\partial \tau_{xz}}{\partial z}=f_x, \tag{2.4a}$$

$$\frac{\partial \sigma_z}{\partial z}+\frac{\partial \tau_{xz}}{\partial x}=f_z, \tag{2.4b}$$

where σ_x and σ_z are the normal stress components in the x- and z-direction, respectively. Here, τ_{xz} is the shear stress, f_x and f_z are the external forces in the x- and z-direction, respectively. The displacement vector is denoted by $\boldsymbol{u}=(u_x,u_z)^\top$ and the infinitesimal strain tensor is defined by

$$\boldsymbol{\epsilon}=\frac{1}{2}\Big(\nabla \boldsymbol{u}+(\nabla \boldsymbol{u})^\top\Big). \tag{2.5}$$

In the current study, we consider the constitutive relation

$$\boldsymbol{\sigma}=\mathbf{D}\,\boldsymbol{\epsilon}, \tag{2.6}$$

where the stress vector $\boldsymbol{\sigma}$ and the constitutive matrix $\mathbf{D}$ are defined by

$$\boldsymbol{\sigma}=\begin{pmatrix}\sigma_x\\ \sigma_z\\ \tau_{xz}\end{pmatrix}, \qquad \mathbf{D}=\frac{E}{(1+\nu)(1-2\nu)}\begin{pmatrix}1-\nu & \nu & 0\\ \nu & 1-\nu & 0\\ 0 & 0 & \dfrac{1-2\nu}{2}\end{pmatrix},$$

with ν is the Poisson ratio and E is the Young modulus characterizing the bed material. Note that we solve the system (2.4), subject to the following boundary conditions.

$$\begin{aligned}&\boldsymbol{\sigma}=\boldsymbol{\sigma}_c, \quad \text{on } \Gamma_i,\\ &\boldsymbol{u}=\mathbf{0}, \quad \text{on } \Gamma,\end{aligned} \tag{2.7a}$$

where Γ is the fixed boundary as shown in Fig. 1. Note that the interface Γ_i between the water and bed depends on time and it is defined as

$$\Gamma_i(t)=\Big\{(x,z)\in\Omega:\ z=B(x,t)\Big\}.$$

The coupled system is numerically solved using a splitting operator where the bed deformation and the water free-surface are computed separately, using the two-dimensional elastostatic equations and the one-dimensional shallow water equation, respectively. The coupling is achieved through the interface Γ_i by updating the bed topography $B(x,t)$ at each deformation step and applying frictional forces f_x and f_z generated from the water flow on Γ_i. Initially, the coupled system is at equilibrium rest and a sudden force is applied on the bed topography to generate a deformation and consequently perturbations are expected to appear on the water free-surface. During the time process, interchange conditions are transferred from the bed topography to the water flow and vice versa. It should also be stressed that in the present study, we assume that bed deformations occur suddenly which lead to a fast characteristic time-scale associated with the propagation of acoustic waves and therefore there is no need to consider the elastodynamics form Eps. (2.4).

3 Coupled finite element/finite volume method

For the numerical solution of the coupled system we consider a finite element method for the two-dimensional elasticity equations (2.4) and a finite volume method for the one-dimensional shallow water equations (2.1). The starting point for the finite element method is the variational formulation of the strain energy in the domain Ω. Thus, multiplying the strong form of x-direction equation in (2.4) by an arbitrary weight function ϕ_x and integrate over the domain yields

$$\int_\Omega \frac{\partial \sigma_x}{\partial x}\phi_x\,d\boldsymbol{x}+\int_\Omega \frac{\partial \tau_{xz}}{\partial z}\phi_x\,d\boldsymbol{x}-\int_\Omega f_x\phi_x\,d\boldsymbol{x}=0.$$

Using the Green-Gauss theorem, the above equation becomes

$$\oint_{\partial\Omega}\sigma_x n_x\phi_x\,d\boldsymbol{x}-\int_\Omega \frac{\partial \phi_x}{\partial x}\sigma_x\,d\boldsymbol{x}+\oint_{\partial\Omega}\tau_{xz}n_z\phi_x\,d\boldsymbol{x}-\int_\Omega \frac{\partial \phi_x}{\partial z}\tau_{xz}\,d\boldsymbol{x}-\int_\Omega f_x\phi_x\,d\boldsymbol{x}=0,$$

where $\boldsymbol{x}=(x,z)^\top$ and $\mathbf{n}=(n_x,n_z)^\top$ is the outward unit normal on $\partial\Omega$ with $\partial\Omega=\Gamma\cup\Gamma_i$. Using the x-component of the traction $\mathcal{T}_x=\sigma_x n_x+\tau_{xz}n_z$, the above equation can be written as

$$\oint_{\partial\Omega}\mathcal{T}_x\phi_x\,d\boldsymbol{x}-\int_\Omega\left(\frac{\partial \phi_x}{\partial x}\sigma_x+\frac{\partial \phi_x}{\partial z}\tau_{xz}\right)d\boldsymbol{x}-\int_\Omega f_x\phi_x\,d\boldsymbol{x}=0. \tag{3.1}$$

Similar steps applied to the z-direction equation in (2.4) give

$$\oint_{\partial\Omega}\mathcal{T}_z\phi_z\,d\boldsymbol{x}-\int_\Omega\left(\frac{\partial \phi_z}{\partial x}\tau_{xz}+\frac{\partial \phi_z}{\partial z}\sigma_z\right)d\boldsymbol{x}-\int_\Omega f_z\phi_z\,d\boldsymbol{x}=0, \tag{3.2}$$

where $\mathcal{T}_z=\sigma_z n_z+\tau_{xz}n_x$. Adding the two equations (3.1) and (3.2) yields

$$\oint_{\partial\Omega}(\mathcal{T}_x\phi_x+\mathcal{T}_z\phi_z)\,d\boldsymbol{x}-\int_\Omega(f_x\phi_x+f_z\phi_z)\,d\boldsymbol{x}-\int_\Omega\left(\frac{\partial \phi_x}{\partial x}\sigma_x+\frac{\partial \phi_x}{\partial z}\tau_{xz}+\frac{\partial \phi_z}{\partial z}\sigma_z+\frac{\partial \phi_z}{\partial x}\tau_{xz}\right)d\boldsymbol{x}=0,$$

which can be reformulated in a vector form as

$$\int_\Omega \widehat{\boldsymbol{\phi}}\cdot\boldsymbol{\sigma}\,d\boldsymbol{x}=\oint_{\partial\Omega}\boldsymbol{\phi}^\top\cdot\boldsymbol{\mathcal{T}}\,d\boldsymbol{x}+\int_\Omega\boldsymbol{\phi}^\top\cdot\mathbf{f}\,d\boldsymbol{x}, \tag{3.3}$$

where $\boldsymbol{\phi}=(\phi_x,\phi_z)^\top$, $\boldsymbol{\mathcal{T}}=(\mathcal{T}_x,\mathcal{T}_z)^\top$ and $\widehat{\boldsymbol{\phi}}=\left(\frac{\partial\phi_x}{\partial x},\frac{\partial\phi_z}{\partial z},\frac{\partial\phi_x}{\partial z}+\frac{\partial\phi_z}{\partial x}\right)^\top$. To solve the weak form (3.3) with the finite element method, the domain Ω is discretized into a set of elements where the solution is approximated in terms of the nodal values U_j and the polynomial basis functions $N_j(x,z)$ as

$$\boldsymbol{u}(x,z)=\sum_{j=1}^{N_d}\mathbf{U}_jN_j(x,z), \tag{3.4}$$

where N_d is the number of mesh nodes. In the present work, we consider quadratic triangular elements with six nodes for which the element displacement $\boldsymbol{u}^e=(u_x^e,u_z^e)^\top$ can be obtained by

$$\boldsymbol{u}^e=\begin{pmatrix} N_1^e & 0 & N_2^e & 0 & \dots & 0\\ 0 & N_1^e & 0 & N_2^e & \dots & N_6^e\end{pmatrix}\begin{pmatrix} u_{x1}\\ u_{z1}\\ u_{x2}\\ u_{z2}\\ \vdots\\ u_{x6}\\ u_{z6}\end{pmatrix},$$

where N_j^e are the shape functions written in local coordinates $(\xi_1,\xi_2)^\top$ as

$$\begin{aligned}
&N_1^e(\xi_1,\xi_2)=\xi_2(2\xi_2-1), && N_2^e(\xi_1,\xi_2)=\xi_1(2\xi_1-1),\\
&N_3^e(\xi_1,\xi_2)=(1-\xi_1-\xi_2)(1-2\xi_1-2\xi_2), && N_4^e(\xi_1,\xi_2)=4\xi_2\xi_1,\\
&N_5^e(\xi_1,\xi_2)=4\xi_1(1-\xi_2-\xi_1), && N_6^e(\xi_1,\xi_2)=4(1-\xi_2-\xi_1)\xi_2.
\end{aligned}$$

To solve the fully discretized problem, the elementary matrices are assembled into a global system of equations

$$\mathbf{K}\boldsymbol{u}=\boldsymbol{b}, \tag{3.5}$$

where $\mathbf{K}$ is the global stiffness matrix, $\boldsymbol{u}$ is the nodal displacement vector and $\boldsymbol{b}$ is the force vector. In our simulations, the matrix $\mathbf{K}$ is decomposed into an $LUL^\top$ factorization, then the solution is reduced to backward/forward substitutions after updating the right-hand side vector $\boldsymbol{b}$ at every time step.

The second step in the considered coupling system is to solve for water perturbations based on the sudden changes on the bed and update the water height and velocity at each time step. For this purpose, we use a finite volume method of Roe type over non-uniform grids to avoid interpolation procedures at the interface Γ_i. A similar method

has been investigated for shallow water equations in [3]. Hence, to formulate the finite volume method we rewrite Eps. (2.1) in conservative form as

$$\frac{\partial \mathbf{W}}{\partial t}+\frac{\partial \mathbf{F}(\mathbf{W})}{\partial x}=\mathbf{Q}(\mathbf{W})+\mathbf{S}(\mathbf{W}), \tag{3.6}$$

where

$$\mathbf{W}=\begin{pmatrix} h \\ \\ hv \end{pmatrix}, \qquad \mathbf{F}(\mathbf{W})=\begin{pmatrix} hv \\ \\ hv^2+\frac{1}{2}gh^2 \end{pmatrix},$$

$$\mathbf{Q}(\mathbf{W})=\begin{pmatrix} 0 \\ \\ -gh\dfrac{\partial B}{\partial x} \end{pmatrix}, \qquad \mathbf{S}(\mathbf{W})=\begin{pmatrix} 0 \\ \\ -gM_b^2h\dfrac{v|v|}{h^{\frac{4}{3}}} \end{pmatrix}.$$

For the time integration of the system (3.6) we divide the time interval into subintervals $[t_n,t_{n+1}]$ with variable size Δt_n such that $t_n=t_{n-1}+\Delta t_n$, $n=1,2,\cdots$ and $t_0=0$. We use the notation $\mathbf{W}^n(x)$ to denote the discrete solution $\mathbf{W}(t_n,x)$. In the current work, we use the splitting operator introduced in [28] to deal with the differential source terms $\mathbf{Q}(\mathbf{W})$ and the non-differential source term $\mathbf{S}(\mathbf{W})$ in (3.6). The splitting procedure consists of the following two steps:

Step 1: Solve for $\widetilde{\mathbf{W}}$

$$\frac{\widetilde{\mathbf{W}}-\mathbf{W}^n}{\Delta t_n}+\frac{\partial \mathbf{F}(\mathbf{W}^n)}{\partial x}=\mathbf{Q}(\mathbf{W}^n). \tag{3.7}$$

Step 2: Solve for $\mathbf{W}^{n+1}$

$$\frac{\mathbf{W}^{n+1}-\widetilde{\mathbf{W}}}{\Delta t_n}=\mathbf{S}\left(\widetilde{\mathbf{W}}\right). \tag{3.8}$$

For the space discretization we discretize the one-dimensional space domain in non-uniform control volumes $\left[x_{i-\frac{1}{2}},x_{i+\frac{1}{2}}\right]$ with length Δx_i and we use the notation $\mathbf{W}_i^n$ to denote the space-averaged of $\mathbf{W}=\mathbf{W}(t,x)$ in the cell $\left[x_{i-\frac{1}{2}},x_{i+\frac{1}{2}}\right]$ at time t_n, and $\mathbf{W}_{i+\frac{1}{2}}^n$ are the intermediate solutions at $x_{i+\frac{1}{2}}$ at time t_n,

$$\mathbf{W}_i^n=\frac{1}{\Delta x_i}\int_{x_{i-\frac{1}{2}}}^{x_{i+\frac{1}{2}}}\mathbf{W}(t_n,x)\,dx, \qquad \mathbf{W}_{i+\frac{1}{2}}^n=\mathbf{W}\left(t_n,x_{i+\frac{1}{2}}\right).$$

Integrating the system (3.7) over the space-time control domain $\left[x_{i-\frac{1}{2}},x_{i+\frac{1}{2}}\right]\times[t_n,t_{n+1}]$, one obtains the following fully discrete system

$$\mathbf{W}_i^{n+1}=\mathbf{W}_i-\frac{\Delta t_n}{\Delta x_i}\left(\mathbf{F}_{i+\frac{1}{2}}^n-\mathbf{F}_{i-\frac{1}{2}}^n\right)+\Delta t_n\mathbf{Q}_i^n, \tag{3.9}$$

where $\mathbf{F}^n_{i\pm\frac{1}{2}} = \mathbf{F}\left(\mathbf{W}^n_{i\pm\frac{1}{2}}\right)$ are the numerical fluxes at $x = x_{i\pm\frac{1}{2}}$ and time $t = t_n$, and $\mathbf{Q}^n_i$ is the space-averaged of the source term $\mathbf{Q}$ defined as

$$\mathbf{Q}^n_i = \frac{1}{\Delta x_i}\int_{x_i-\frac{1}{2}}^{x_i+\frac{1}{2}} \mathbf{Q}(\mathbf{W})\, dx. \tag{3.10}$$

The spatial discretization (3.9) is complete when the numerical fluxes $\mathbf{F}^n_{i\pm1/2}$ and the source term $\mathbf{Q}^n_i$ are reconstructed. Generally, this step can be carried out using any finite volume method developed in the literature for solving hyperbolic systems of conservation laws, see for example [8, 9]. In the present study, we consider the Roe reconstruction defined as [25]

$$\mathbf{F}^n_{i+\frac{1}{2}} = \frac{1}{2}\left(\mathbf{F}(\widehat{\mathbf{W}}^n_{i+1}) + \mathbf{F}(\widehat{\mathbf{W}}^n_i)\right) + \frac{1}{2}\mathbf{A}\left(\widehat{\mathbf{W}}^n_{i+\frac{1}{2}}\right)\left(\widehat{\mathbf{W}}^n_i - \widehat{\mathbf{W}}^n_{i+1}\right), \tag{3.11}$$

where the averaged state $\widehat{\mathbf{W}}^n_{i+\frac{1}{2}}$ is calculated as

$$\widehat{\mathbf{W}}^n_{i+\frac{1}{2}} = \begin{pmatrix} \dfrac{h^n_i + h^n_{i+1}}{2} \\ \dfrac{\sqrt{h^n_i}v^n_i + \sqrt{h^n_{i+1}}v^n_{i+1}}{\sqrt{h^n_i + h^n_{i+1}}} \end{pmatrix}, \tag{3.12}$$

and the Roe matrix in (3.11) is defined as $\mathbf{A} = \mathbf{R}\mathbf{\Lambda}\mathbf{R}^{-1}$ with

$$\mathbf{R} = \begin{pmatrix} 1 & 1 \\ \widehat{\lambda}_1 & \widehat{\lambda}_2 \end{pmatrix}, \qquad \mathbf{\Lambda} = \begin{pmatrix} \widehat{\lambda}_1 & 0 \\ 0 & \widehat{\lambda}_2 \end{pmatrix}, \tag{3.13}$$

with $\widehat{\lambda}_1 = \widehat{v} - \sqrt{g\widehat{h}}$ and $\widehat{\lambda}_2 = \widehat{v} + \sqrt{g\widehat{h}}$ are the two eigenvalues associated with the system evaluated at the averaged state (3.12).

For the discretization of the source term $\mathbf{Q}^n_i$ we implement a well-balanced reconstruction investigated in [3]. Thus, the well-balanced discretization of $\mathbf{Q}^n_i$ is achieved by in splitting the integral in (3.10) over the two sub-cells $\left[x_{i-\frac{1}{2}}, x_i\right]$ and $\left[x_i, x_{i+\frac{1}{2}}\right]$ of the control volume $\left[x_{i-\frac{1}{2}}, x_{i+\frac{1}{2}}\right]$ as

$$\mathbf{Q}^n_i = \frac{1}{\Delta x_i}\left(\frac{(x_i - x_{i-1})}{2}\mathbf{Q}^L_{i-\frac{1}{2}} + \frac{(x_{i+1} - x_i)}{2}\mathbf{Q}^R_{i+\frac{1}{2}}\right), \tag{3.14}$$

where $\mathbf{Q}^L_{i-\frac{1}{2}}$ and $\mathbf{Q}^R_{i+\frac{1}{2}}$ are the space-averaged of the source term $\mathbf{Q}$ in the sub-cells $\left[x_{i-\frac{1}{2}},x_i\right]$ and $\left[x_i,x_{i+\frac{1}{2}}\right]$ defined as

$$\mathbf{Q}^L_{i-\frac{1}{2}}=\begin{pmatrix} 0 \\ \\ -g\dfrac{h_i+h_{i-1}}{2}\left(B_i-B_{i-1}\right) \end{pmatrix}, \qquad \mathbf{Q}^R_{i-\frac{1}{2}}=\begin{pmatrix} 0 \\ \\ -g\dfrac{h_{i+1}+h_i}{2}\left(B_{i+1}-B_i\right) \end{pmatrix}.$$

It is evident that for small water depths, the bed friction term dominates the other terms in the momentum equation. This is mainly due to the presence of the term $h^{\frac{4}{3}}$ in the dominator of τ_f in (2.2). To overcome this drawback we use a semi-implicit time integration of the source term $\mathbf{S}$ in (3.8) as

$$\frac{h^{n+1}-\widetilde{h}}{\Delta t}_n=0, \tag{3.15a}$$

$$\frac{(hv)^{n+1}-\left(\widetilde{h}\widetilde{v}\right)}{\Delta t}_n=-gM_b^2\frac{(hv)^{n+1}|\widetilde{v}|}{\left(\widetilde{h}\right)^{\frac{4}{3}}}, \tag{3.15b}$$

where $\widetilde{h}$ and $\widetilde{v}$ are the water height and velocity obtained from the first step (3.7) of the splitting procedure. Solving the second equation in (3.15) for $(hv)^{n+1}$ yields

$$(hv)^{n+1}=\frac{\left(\widetilde{h}\widetilde{v}\right)}{1+\Delta t_n gM_b^2|\widetilde{v}|\,/\left(\widetilde{h}\right)^{\frac{4}{3}}}. \tag{3.16}$$

As in most explicit time integration schemes, the time step in our finite volume method is selected using a Courant-Friedrichs-Lewy (CFL) condition. In our simulations, the Courant number Cr is fixed and Δt_n is chosen at each time step according to the following CFL condition

$$\Delta t_n=Cr\frac{\min\left(\Delta x_i\right)}{\max\left(\left|\widehat{\lambda}_1^+\right|,\left|\widehat{\lambda}_1^-\right|,\left|\widehat{\lambda}_2^+\right|,\left|\widehat{\lambda}_2^-\right|\right)}, \tag{3.17}$$

where $\widehat{\lambda}_1^{\pm}=\widehat{v}_1^{\pm}-\sqrt{g\widehat{h}_1^{\pm}}$ and $\widehat{\lambda}_2^{\pm}=\widehat{v}_2^{\pm}+\sqrt{g\widehat{h}_2^{\pm}}$ with $\widehat{h}_{1,2}^{\pm}$ and $\widehat{v}_{1,2}^{\pm}$ are computed using the space-averaged solutions in the control volume $\left[x_{i-\frac{1}{2}},x_{i+\frac{1}{2}}\right]$ and its two neighbouring cells as

$$\widehat{h}_1^+=\frac{h_{i+1}+h_i}{2},\quad \widehat{h}_1^-=\frac{h_i+h_{i-1}}{2},\quad \widehat{v}_1^+=\frac{\sqrt{h_{i+1}}v_{i+1}+\sqrt{h_i}v_i}{\sqrt{h_{i+1}}+\sqrt{h_i}},\quad \widehat{v}_2^+=\frac{\sqrt{h_i}v_i+\sqrt{h_{i-1}}v_{i-1}}{\sqrt{h_i}+\sqrt{h_{i-1}}}.$$

Note that the above finite volume method is only first-order accurate. In the present study, we use flux limiters to reconstruct a second-order accurate finite volume method for solving (3.6). The implementation of this method for solving the shallow water equations (2.1) is similar to the one presented in [4] and it is omitted here.

3.1 Implementation of coupling conditions at the interface

One of the advantages in using non-uniform grids in the finite volume solution is to avoid interpolations at the interface for interchange coupling conditions. Here, the selected control volumes in the finite volume methods coincide with the finite element nodes on the interface as shown in Fig. 2. At each time step coupling conditions are transferred on the interface for both models to update the solutions for the displacement $\boldsymbol{u}$, water height h and water velocity v. In the present work, the deformed finite element nodes on the interface are used to reconstruct the bed $B(x,t)$ for the shallow water equations (2.1). Here, a triangular finite element with three nodes on the interface yields two non-uniform control volumes the edges of which are the three nodes and their centers are obtained by averaging the coordinates of these nodes, compare Fig. 2. We also assume that once the deformation occurs, the time variation in these coordinates is negligible and therefore no need for interpolation procedures to reconstruct the bed topography in the finite volume method. This bed profile is used in the finite volume solution of the flow system to obtain the water height h^{n+1} and the water velocity v^{n+1} at the next time level t_{n+1}.

For coupling conditions from the water flow to the bed on the interface, the forces f_x and f_z in the elasticity equations (2.4) are reconstructed at each time step. Here, the horizontal force f_x in the x-direction is updated using the friction term as

$$f_x = -gM_b^2 h^{n+1} \frac{v^{n+1}\left|v^{n+1}\right|}{\left(h^{n+1}\right)^{\frac{4}{3}}}. \tag{3.18}$$

The vertical force f_z in the z-direction is reconstructed at each time step using the change in the hydrostatic pressure as

$$p^{n+1} = -\rho g \frac{h^{n+1}-h^n}{\Delta t_n}$$

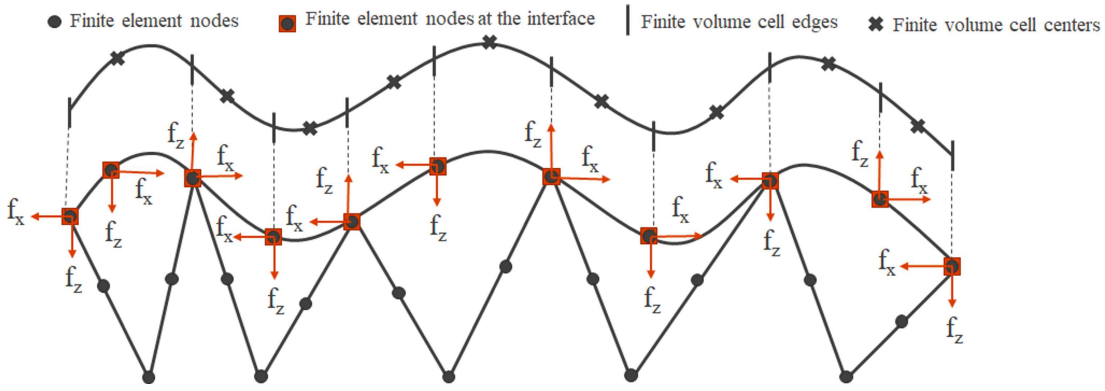

Figure 2: A schematic illustration of finite element and finite volume nodes at the interface.

Algorithm 1 Coupled finite element/finite volume method used in the present study.

Require: T the final simulation time.

1: Assemble the stiffness matrix $\mathbf{K}$ for elastostatic system using the finite element method (3.1)-(3.5).
2: **while** $t_n \leqslant T$ **do**
3: Assemble the force vector $\mathbf{b}$ for elastostatic system using the finite element method (3.1)-(3.5).
4: Solve the linear system (3.5) for the displacement in the computational mesh.
5: Update the displacement of the finite element nodes on the interface.
6: Reconstruct the bed B on the control volumes formed by the finite element nodes on the interface.
7: Update the time step Δt_n according to the CFL condition (3.17).
8: Solve the shallow water equations using:
9: **for** each control volume $\left[x_i, x_{i+\frac{1}{2}}\right]$ **do**
10: Compute the numerical fluxes $\mathbf{F}^n_{i+\frac{1}{2}}$ using the Roe scheme (3.11).
11: Discrete the source term $\mathbf{Q}_i$ using the well-balanced discretization (3.14).
12: Compute the solution in the first stage of the splitting $\mathbf{W}_i^{n+1}$ using (3.9).
13: Update the solution in the second stage of the splitting (3.8) using (3.15)-(3.16).
14: **end for**
15: Compute the horizontal force f_x using the bed friction according to (3.18).
16: Compute the vertical force f_z using the hydrostatic pressure according to (3.19).
17: Overwrite $t_n \longleftarrow t_n + \Delta t_n$ and go to step 2.
18: **end while**

and at each node of the three finite element nodes located on the interface, the force f_z is distributed using the integral form as

$$f_z^{(1)} = \int_{-1}^{1} -\frac{1}{2}\xi(1-\xi)\, p^{n+1}\frac{\hbar}{2}\, d\xi = \frac{1}{6}p^{n+1}\hbar, \tag{3.19a}$$

$$f_z^{(2)} = \int_{-1}^{1} \left(1-\xi^2\right) p^{n+1}\frac{\hbar}{2}\, d\xi = \frac{2}{3}p^{n+1}\hbar, \tag{3.19b}$$

$$f_z^{(3)} = \int_{-1}^{1} \frac{1}{2}\xi(1+\xi)\, p^{n+1}\frac{\hbar}{2}\, d\xi = \frac{1}{6}p^{n+1}\hbar, \tag{3.19c}$$

where $\hbar$ is the edge length of the considered element on the interface. It is easy to verify that $f_z^{(1)} + f_z^{(2)} + f_z^{(3)} = p^{n+1}\hbar$. The total force f_z in the z-direction is obtained by accumulating the elemental forces on the overlapping nodes, see Fig. 2 for an illustration. In summary, the coupled finite element/finite volume method proposed in this study to solve shallow water waves by elastic deformations in the topography is carried out in the steps described in Algorithm 1.

4 Numerical results and examples

In this section we examine the performance of the proposed computational model introduced in the above sections using several examples of shallow water waves by elastic deformations in the topography. For the first test example, we verify the accuracy of the techniques described in this study for two well-established test examples of shallow water flows and elastostatic deformations. In all the computations reported in this section unless stated otherwise, the Youngs modulus $E=10000\,Mpa$, the Poison ratio $\nu=0.3$, the gravitational acceleration $g=9.81\,m/s^2$ and the Manning coefficient $M_b=0.025\,s/m^{1/3}$. Here, the Courant number is fixed to $Cr=0.85$ and the time stepsize Δt_n is adjusted at each time step according to the stability condition (3.17). All the computations were performed on an Intel® Core(TM) i7-7500U @ 2.70GHz with 16 GB of RAM.

4.1 Accuracy test examples

We examine the accuracy of both the finite element and finite volume methods for two well-established test examples. First we consider a dam-break problem with known analytical solution. Here, we solve the shallow water equations (2.1) over a frictionless flat bottom in the domain $[0,1]$ with initial conditions defined as

$$h(x,0)=\begin{cases}1.0, & \text{if } x\leq 0.5,\\ 0.5, & \text{elsewhere,}\end{cases}\qquad v(x,0)=0.$$

At $t=0$, the dam collapses and the flow problem consists of a shock wave traveling downstream and a rarefaction wave traveling upstream. The analytical solution of this problem is given by [2]

$$h(x,t)=\begin{cases}1, & \text{if } x<\dfrac{1}{2}-t\sqrt{g},\\ \dfrac{1}{9g}\left(2\sqrt{g}-\dfrac{2x-1}{2t}\right)^2, & \text{if } \dfrac{1}{2}-t\sqrt{g}\leq x\leq (u_2-c_2)t+\dfrac{1}{2},\\ \dfrac{1}{4}\sqrt{1+\dfrac{16C_s^2}{g}}-1), & \text{if } (u_2-c_2)t+\dfrac{1}{2}<x\leq C_st+\dfrac{1}{2},\\ \dfrac{1}{2}, & \text{if } C_st+\dfrac{1}{2}<x,\end{cases}$$

where

$$u_2=C_s-\frac{g}{8C_s}\left(1+\sqrt{1+\frac{16C_s^2}{g}}\right),\quad c_2=\sqrt{\frac{g}{4}\left(\sqrt{1+\frac{16C_s^2}{g}}-1\right)},\quad C_s=2.957918120187525.$$

In Fig. 3 we compare numerical results obtained for the water height at time $t=0.1$ using the proposed finite volume method on uniform and non-uniform meshes with 50 and

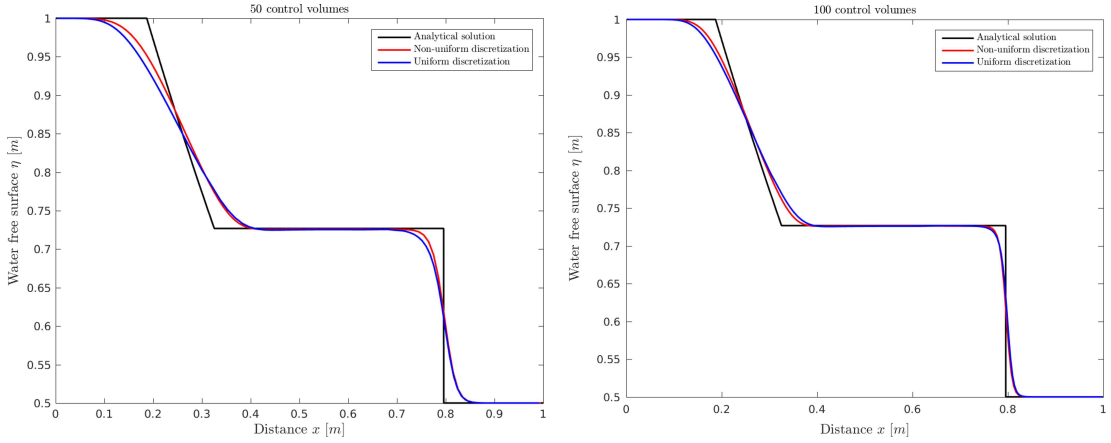

Figure 3: Results obtained using the finite volume method on uniform and non-uniform meshes using 50 control volumes (left) and 100 control volumes (right).

100 control volumes. Notice that for the uniform meshes, the spatial step $\Delta x = 0.02$ and $\Delta x = 0.01$ for the meshes with 50 and 100 control volumes, respectively. In the non-uniform meshes, the spatial step Δx_i is selected as

$$\Delta x_i = \begin{cases} 0.016, & \text{if } 0.3 \le x_i \le 0.7, \\ 0.03, & \text{elsewhere,} \end{cases} \quad \text{and} \quad \Delta x_i = \begin{cases} 0.008, & \text{if } 0.3 \le x_i \le 0.7, \\ 0.015, & \text{elsewhere.} \end{cases}$$

It is clear from the results in Fig. 3 that refining the mesh improves the accuracy of the numerical results on both uniform and non-uniform meshes. Compared to the analytical solution, results obtained using non-uniform meshes are slightly more accurate than those obtained on the uniform mesh. For instance, the numerical diffusion is more pronounced at the shock and rarefaction areas in the uniform results than in their non-uniform counterparts. These features are important when the shallow water equations are solved on the non-uniform meshes reconstructed directly from the finite element nodes located on the interface in the coupled model. This would avoid interpolation procedures for matching finite element and finite volume nodes on the interface which may introduce numerical diffusion in the results obtained for the free-surface solutions.

Next we verify the finite element method for solving two-dimensional elasticity problems. We consider the well-known example proposed in [22] and for which the exact solution is provided therein. Here, we solve the elasticity equations (2.4) in a homogeneous and isotropic rectangular domain with $100\,m$ for the length and $10\,m$ for the width. A nodal displacement of $3\,m$ is applied upwards in the center point of the domain and results obtained for the horizontal and vertical displacements are compared to the exact solutions. The computational domain is discretized using quadratic finite elements in an unstructured mesh with 772 elements and 1649 nodes. Fig. 4 illustrates the obtained results for the horizontal and vertical displacements compared to the exact solutions.

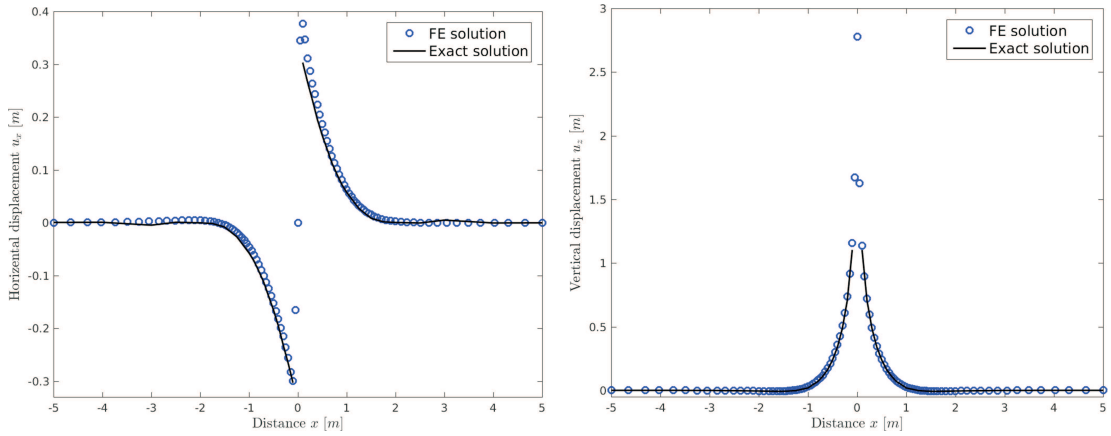

Figure 4: Horizontal displacement (left) and vertical displacement (right) obtained for the accuracy test example using the finite element method.

There is a good agreement between the results obtained using the finite element method and the analytical solutions for both horizontal and vertical displacements. The finite element method performs well for this test example and produces highly accurate and stable numerical results using reasonably coarse meshes.

4.2 Shallow water waves generated by tension in the topography

In this example we consider shallow water waves generated by tension in the topography of a rectangular domain $100\,m$ long and $10\,m$ high subject to a localized tension force of $F=2000\,N$ acting on the surface area between $x=47m$ and $x=53m$. Initially, the system is at rest with a water height set to $h=10\,m$ and velocity $v=0\,m/s$. Both open flow and reflective boundary conditions are imposed at both ends of the domain to model open and close flow domains, respectively. At time $t=0.1\,s$, the considered force is applied generating a sudden deformation in the bed topography. The finite element nodes located on the interface are used for the control volumes in the finite volume solution of the shallow water equations. First we examine the grid convergence in the proposed coupled finite element/finite volume method for this example. To this end, we consider five unstructured meshes with different node and element densities as depicted Fig. 5. Their corresponding statistics are listed in Table 1 along with the CPU times obtained using Mesh A, Mesh B, Mesh C, Mesh D and Mesh E. Note that, to avoid refining the mesh everywhere in the elastic domain, only the area subject to the deformation is refined in our computational mesh. This would require less computational cost than considering a uniformly fine mesh in the simulations. A very fine reference mesh with 39591 elements and 80036 nodes is also used in our simulations to quantify errors in the obtained solutions obtained at time $t=3\,s$. Note that the reference mesh is not included in Fig. 5 because of its density which results in a heavily black plot. As can be seen for the last two

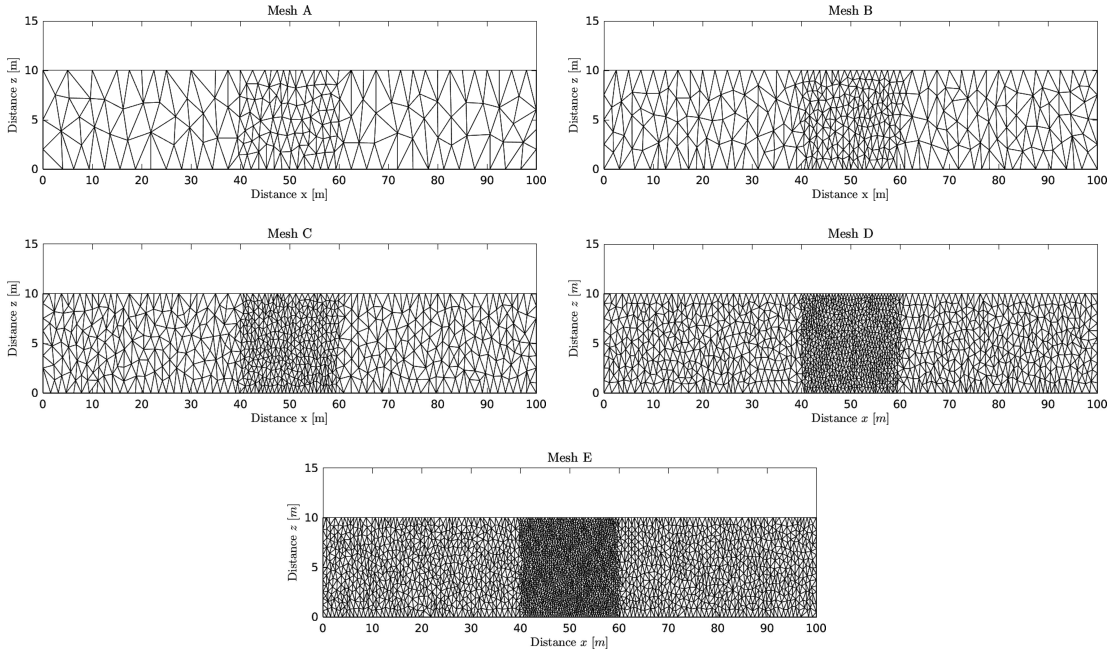

Figure 5: Meshes used in the simulations for shallow water waves generated by tension in the topography.

Table 1: Mesh statistics, relative errors and computational times for shallow water waves generated by tension in the topography at time $t=3s$. The CPU times are given in seconds.

	# elements	# nodes	# control volumes	Error in σ_x	Error in η	CPU time
Mesh A	312	709	78	1.473E-02	3.205E-01	6.5
Mesh B	620	1349	96	4.289E-03	1.741E-01	9.2
Mesh C	1236	2639	197	1.157E-03	9.329E-02	21.7
Mesh D	2471	5160	232	2.994E-04	3.788E-02	63.4
Mesh E	4940	10213	312	7.433E-05	1.339E-02	131.5

mesh levels Mesh D and Mesh E, the differences in errors obtained for the stresses σ_x and free-surface η in Table 1 are very small. To further qualify the results for these meshes we plot in Fig. 6 the bed profiles obtained using the considered meshes. It is easy to see that solutions obtained using the Mesh A are far from those obtained by the other meshes. Increasing the density of elements, the results for the Mesh D and Mesh E are roughly similar. Results obtained for the stresses σ_x and σ_z and not reported here for brevity, show the same trends. This ensures grid convergence of the numerical results. Hence, the Mesh D is used in all our next computations. The reasons for choosing this mesh structure lie essentially on the computational cost required for each mesh configuration and also on the numerical resolution obtained.

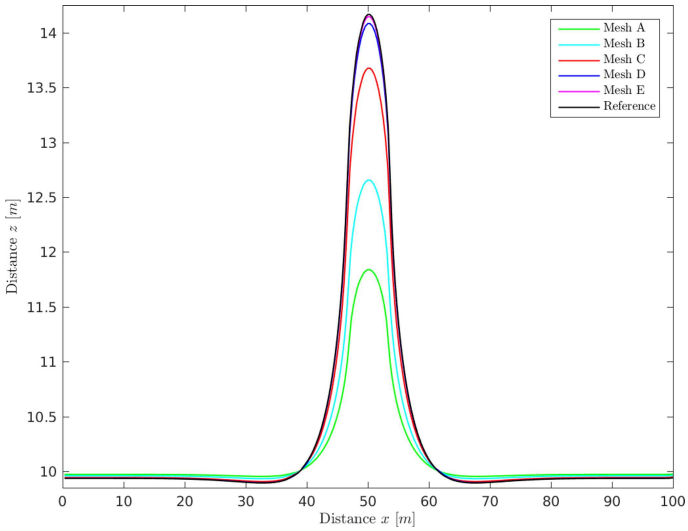

Figure 6: Comparison of bed profiles using different meshes for shallow water waves generated by tension in the topography at time $t=3s$.

The unstructured finite element with 2471 elements and 5160 nodes is used in the simulations and the results are monitored for different instants. The associated number of control volumes for this finite element mesh is 195 non-uniform cells. In Fig. 7 we display the obtained results for the water height and bed deformation at six different times namely, $t=0\,s$, $0.1\,s$, $1\,s$, $2\,s$, $3\,s$ and $10\,s$ using open flow boundary conditions at both upstream and downstream. These plots give a clear view of the overall wave patterns and the effect of the bed deformation on the structure of the propagating waves in the upstream and downstream of the domain. In addition to the primary wave, a pair of waves with the same amplitude develops in both side of the hump. As expected, the sudden deformation in the bed generates a wave propagating across the computational domain. The wave splits into two waves and in later times the waves leave the domain and the water free-surface becomes flat at the initial height. This confirms the well-balanced property of the proposed finite volume method on non-uniform meshes. It is also important to mention two points concerning the non-uniform control volumes used in the flow simulations. First, there is no need for interpolation procedures to pass the information from one mesh to another in our coupled finite element/finite volume method second, there is no need to refine the mesh in the finite volume method to resolve the wave fronts as the finite element mesh would generate these refined meshes. This is a remarkable feature of the proposed coupled finite element/finite volume method to satisfactorily handle procedures using adaptive local grid refinement methods to resolve free-surface wave problems.

Fig. 8 illustrates the distribution of the stresses σ_x and σ_z at time $t=3\,s$. Obviously, high stresses appear at the hump where the bed deformation is taken place. The perfect

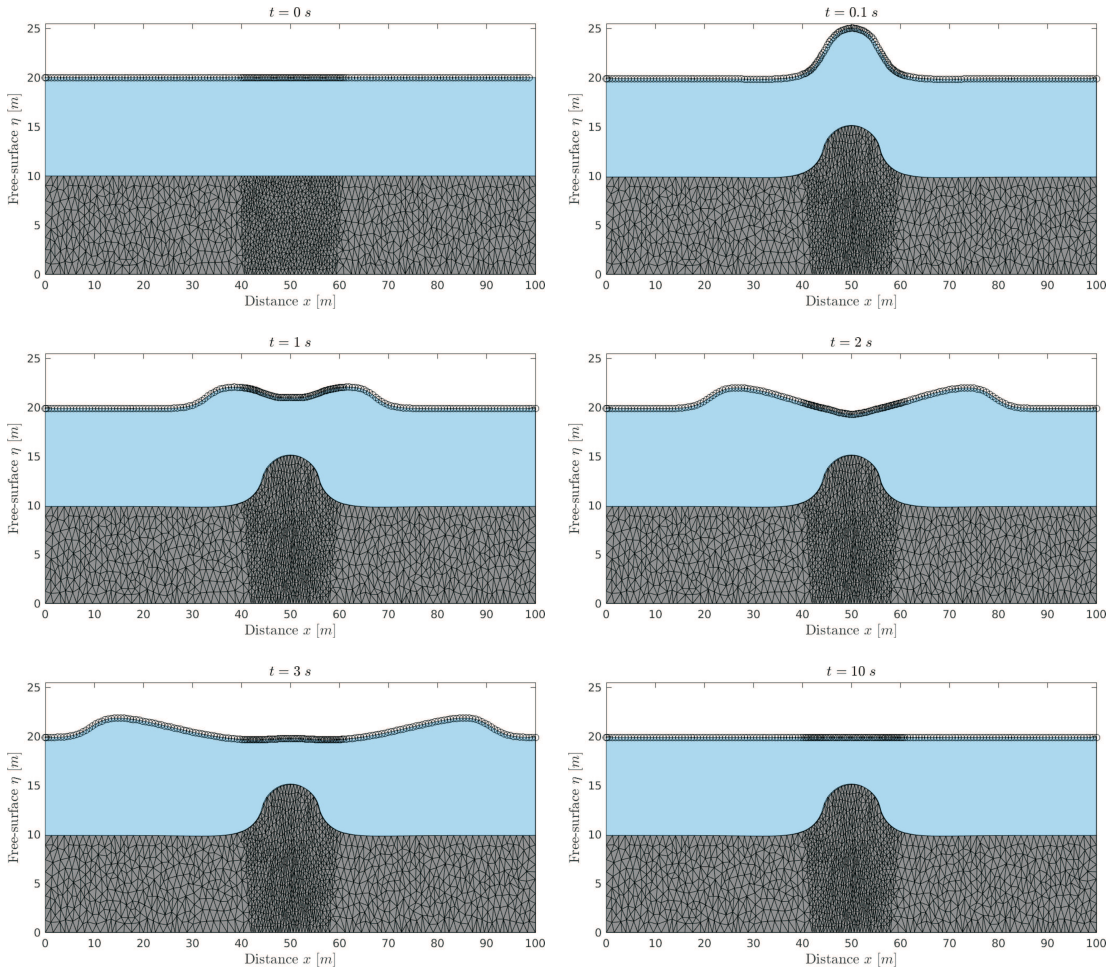

Figure 7: Results for the water height and bed deformation obtained for shallow water waves generated by tension in the topography at six different times.

symmetry in these results with respect to the vertical centerline should be noted. Our finite element method preserves the symmetry in the stresses and resolves the correct solution well for this test example. For this example, we also consider the close domain with reflective boundary conditions at both upstream and downstream. In this case we compute the total water head for as

$$H = B + h + \frac{v^2}{2g}. \tag{4.1}$$

In Fig. 9 we present the time evolution of the total water head at three surface gauges G_1, G_2 and G_3 situated at $x = 20\,m$, $x = 50\,m$ and $x = 80\,m$, respectively. The total water head obtained at these locations fluctuates with different amplitudes and frequencies but

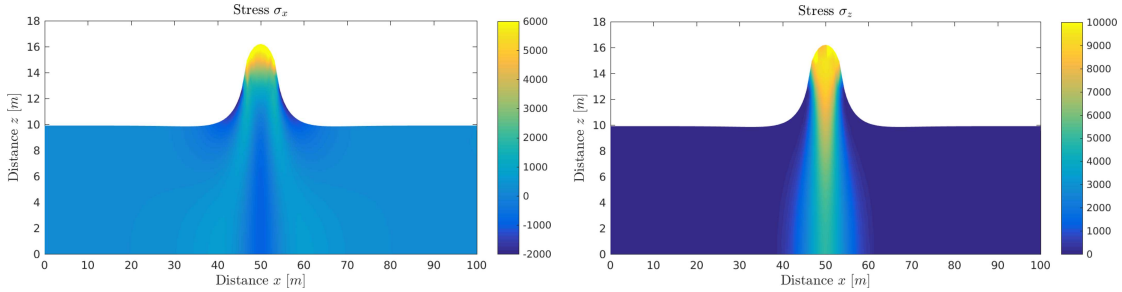

Figure 8: Distribution of the stresses σ_x (left) and σ_z (right) obtained for shallow water waves generated by tension in the topography at $t=3s$.

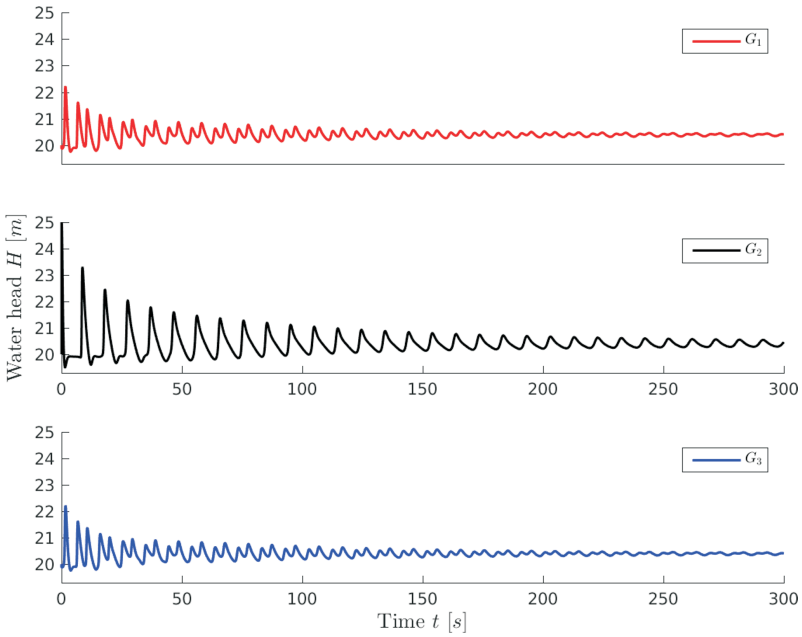

Figure 9: Time evolution of the total water head at the three gauges G_1, G_2 and G_3 obtained for shallow water waves generated by tension in the topography.

at later time it stabilizes at the same initial value for the three considered gauges. The highest amplitudes in the total water head are observed at the gauge G_2 which is located at the center where the deformation occurs. Because of the symmetry in the location of gauges G_1 and G_3, the total water head at these locations exhibits similar features in terms of amplitudes and frequencies. In all selected gauges, the coupled finite element/finite volume method maintains correctly the wave structures without any kind of spurious oscillations over the hump.

We also examine the effects of the applied force on the generated waves for this test example. Hence, in Fig. 10 we show the bed deformations at time $t=0.1\,s$ and the time

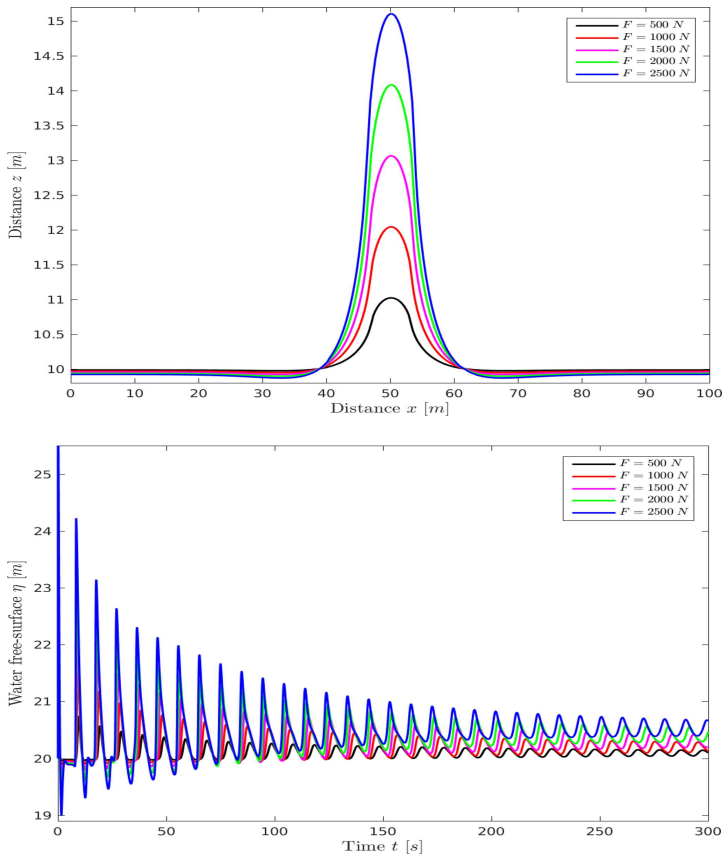

Figure 10: Bed deformation (top) time evolution of the free-surface at the gauge G_2 (bottom) obtained for shallow water waves generated by tension in the topography using different values of the tension force.

evolution of the water free-surface at the gauge G_2 obtained using different values of the tension force namely, $F = 500\,N$, $1000\,N$, $1500\,N$, $2000\,N$ and $2500\,N$. To further quantify the results for this case we summarize in Table 2 the maximum values of the stress σ_z, the stress σ_x, the bed B, the free-surface η, and the hydrostatic pressure p. It is clear high responses in both bed and free-surface are obtained for high values of the tension force. It should be pointed out that the performance of the proposed method is very attractive since the obtained numerical solutions remain stable and conservative even when coarse meshes are used in the simulations without requiring nonlinear solvers or complicated techniques to reconstruct the numerical fluxes in the shallow water equations.

4.3 Shallow water waves generated by tension-compression in the topography

This example considers the same configuration as in the previous problem but using both tension and compression forces on the bed topography. Thus, a force of $2000\,N$ is applied

Table 2: Computational results for shallow water waves generated by tension in the topography using different values of the tension force.

Force (N)	maxσ_z (KPa)	maxσ_x (KPa)	max$B$ (m)	maxη (m)	max$p$ (KN/m^2)
500	1.965	1.23	11.0335	21.1815	97.2559
1000	3.931	2.4599	12.0670	23.4026	106.5393
1500	5.8951	3.6899	13.1005	25.6435	115.9026
2000	7.8602	4.9198	14.1099	27.8662	125.1387
2500	9.8252	6.1498	15.3791	30.0551	134.1614

as a tension in the surface area between $x=28\,m$ and $x=32\,m$, and as a compression in the surface area between $x=78m$ and $x=82m$ in the computational domain. Initially, the system is assumed at the equilibrium with the water height set to $h=11m$ and the velocity $v=0\,m/s$. For the boundary conditions, open flow and reflective conditions are imposed at both ends of the domain. The solid domain is discretized using an unstructured mesh with local refinements in the areas where tension and compression forces are applied. The total numbers of elements and nodes in this mesh are 3417 and 7086, respectively. This results in 193 non-uniform control volumes to be used in the finite volume method. Note that, to break in the symmetry in this problem, the forces are applied in areas with different distances to the centerline $x=50\,m$.

The considered tension and compression forces are applied at time $t=0.1s$ and a sudden deformation occurs in the bed topography. After each deformation step, the finite volume solution of the shallow water equations uses the non-uniform control volumes obtained from the finite element nodes located on the interface. Fig. 11 presents the obtained results for the bed deformation and water height at six different times namely, $t=0\,s$, $0.1\,s$, $1\,s$, $4\,s$, $5\,s$ and $17\,s$ using open flow boundary conditions at both ends of the channel. As can be seen, the tension and compression forces generate two water waves with different crests and troughs propagating along the computational domain. The interaction between these waves generates reflecting waves with different amplitudes in the water free-surface. At later time, the waves are settled out and the system returns to its initial equilibrium state. Again, the proposed coupled finite element/finite volume method performs well for this test problem as the deformed bed topography is accurately resolved using the finite element method and the wave features are well captured using the finite volume method on non-uniform meshes.

In Fig. 12 we show distributions of the computed stresses σ_x and σ_z at time $t=5\,s$. It is clear that high stresses are localized at the hump generated from the tension force whereas, low stresses appear at the scour resulting from the compression force. The results also show different aspects in the stresses generated by tension force and those obtained using the compression force. The finite element method performs well for this deformation test example and it reproduces stable solutions without nonphysical oscillations at the bed topography and at stress distributions. The total water head H defined

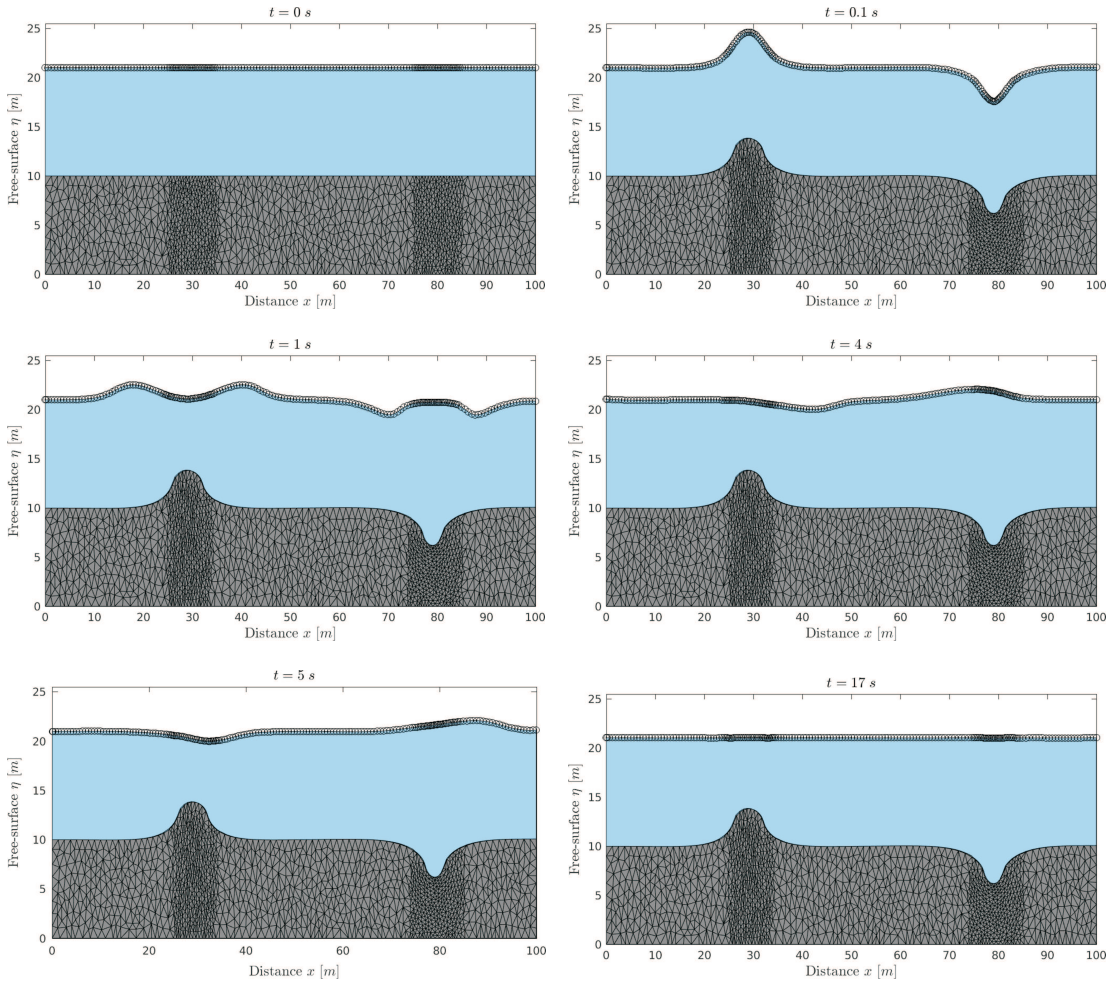

Figure 11: Results for the water height and bed deformation obtained for shallow water waves generated by tension-compression in the topography at six different times.

in (4.1) is also considered for this test example using reflective boundary conditions at both ends of the domain. Fig. 13 shows the time evolution of the total water head at three selected gauges G_1, G_2 and G_3 at $x = 30\,m$, $x = 50\,m$ and $x = 80\,m$, respectively. Unlike the previous example, the time series in the present case exhibit periodic behavior with low amplitudes and frequencies. In addition, compared to the previous case, the propagating waves generated by both tension and compression in the topography persist longer on the free-surface than in those originated by tension only. It is clear that the total water head experiences high values at the gauge G_1 located at the downstream of the domain. The coupled finite element/finite volume method captures well the periodic features in the water waves at all selected gauges for this example.

This test example is also used to assess effects of the Poisson ratio ν on the bed defor-

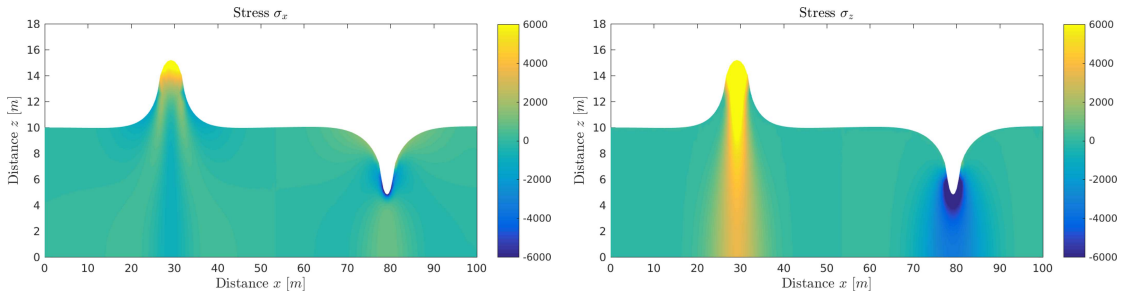

Figure 12: Distribution for the stresses σ_x (left) and σ_z (right) obtained for shallow water waves generated by tension-compression in the topography at $t=5s$.

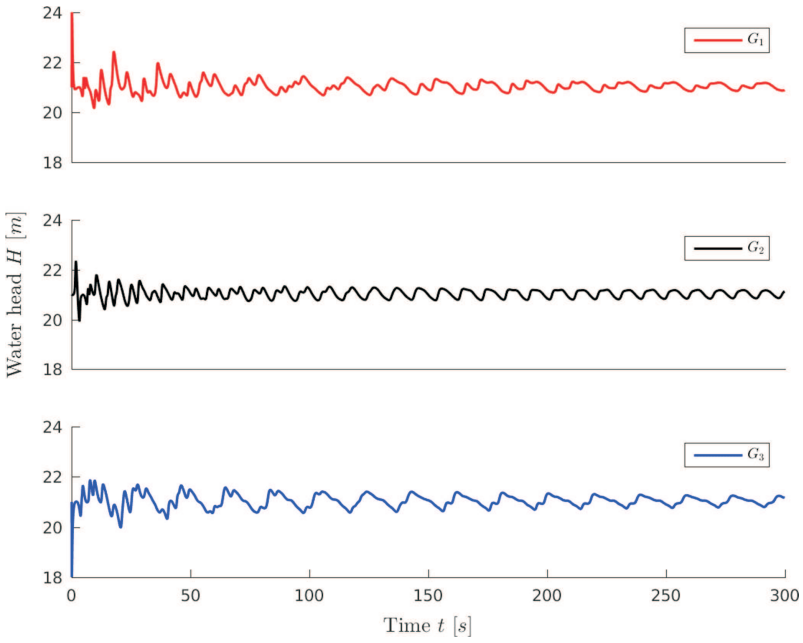

Figure 13: Time evolution of the total water head at the three gauges G_1, G_2 and G_3 obtained for shallow water waves generated by tension-compression in the topography.

mation and the generated free-surface waves. To this end, we run the simulations for the bed formed by different homogeneous and isotropic materials with $\nu=0.1$, 0.2, 0.3 and 0.4. In Fig. 14 we display the bed deformations at time $t=0.1\,s$ and the time evolution of the water free-surface at the gauge G_1 obtained using the considered values of the Poisson ratio. The maximum values of the stress σ_z, the stress σ_x, the bed B, the free-surface η and the hydrostatic pressure p are summarized in Table 3. As can be seen from these results, slightly high responses in both bed topography and free-surface are obtained for low values of the Poisson ratio, compare the results for $\max B$ in Table 3.

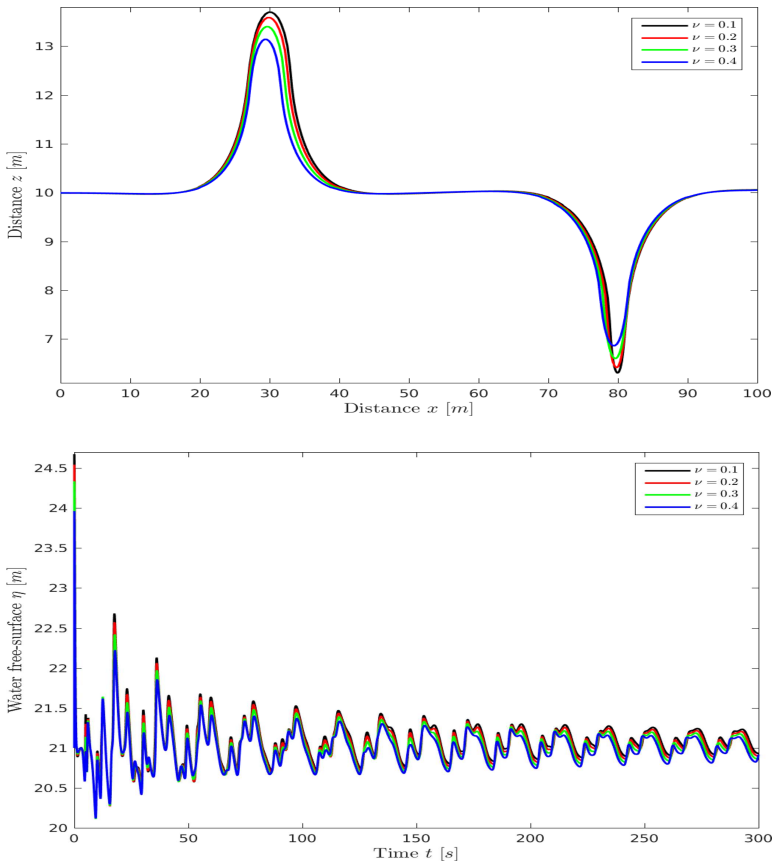

Figure 14: Bed deformation (top) time evolution of the free-surface at the gauge G_1 (bottom) obtained for shallow water waves generated by tension-compression in the topography using different values of the Poisson ratio.

Table 3: Computational results for shallow water waves generated by tension-compression in the topography using different values of the Poisson ratio.

ν	$\max\sigma_z$ (KPa)	$\max\sigma_x$ (KPa)	$\max B$ (m)	$\max\eta$ (m)	$\max p$ (KN/m^2)
0.1	7.265	5.6249	13.6954	27.3934	134.0797
0.2	7.3601	5.4965	13.5848	27.1569	132.7335
0.3	7.5260	5.2995	13.3993	26.5743	129.3346
0.4	7.8963	5.0911	13.1385	26.1080	126.7165

4.4 Shallow water waves generated by pipe failure in the topography

Pipe failures are among common examples in nature for which several studies have taken place in civil engineering and geotechnics, see for example [10, 16, 36]. For these applications, the source of deformation may be caused by a fatigue in the pipe or simply by a

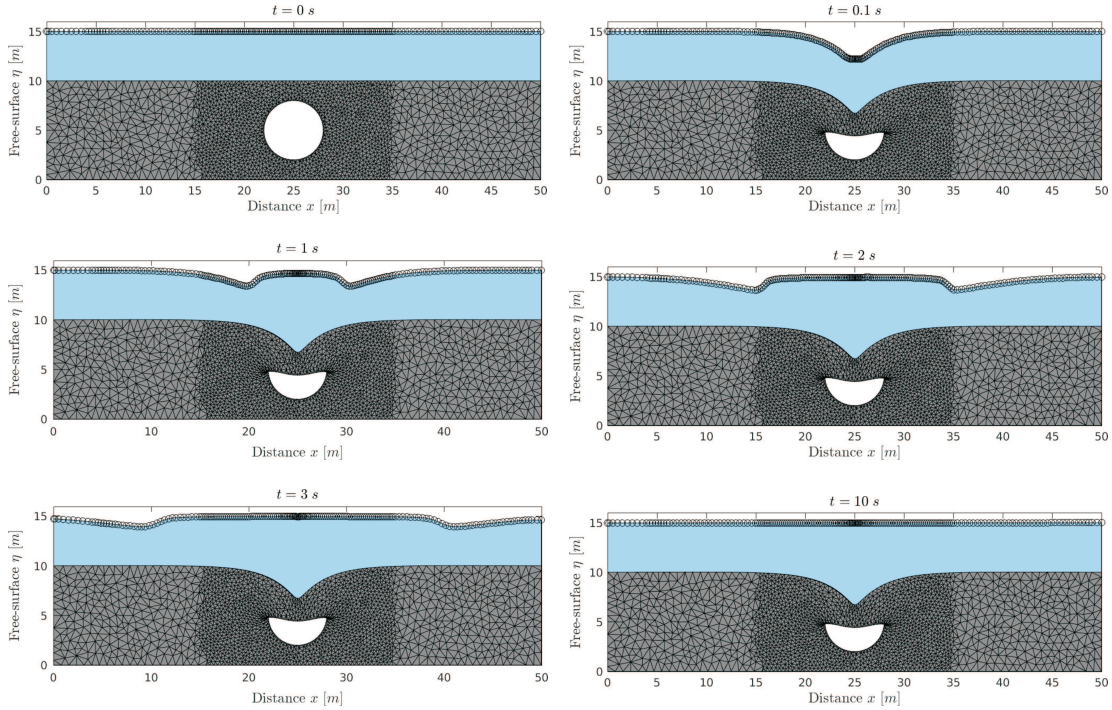

Figure 15: Results for the water height and bed deformation obtained for shallow water waves generated by pipe failure in the topography at six different times.

load applied below the seabed. In this example, we consider shallow water waves generated by pipe failure in the bed topography. Hence, we solve the coupled equations (2.1) and (2.4) in a rectangular domain $50\,m$ long and $10\,m$ high including a circular pipe with radius $R=3\,m$ and the initial water height is $5\,m$ above the bed. A compressive force of $200\,N$ is applied only at the upper half boundary of the pipe. Initially, the system is at rest and at time $t=0.1\,s$ the constant force is applied on the upper surface of the pipe. Consequently a deformation is expected on the pipe and therefore on the shallow water bed which generate water waves on the free-surface. An unstructured finite element mesh with 3196 elements and 6822 nodes is used in our simulations and numerical results are presented for different instants. To avoid refining the mesh everywhere in the computational domain, only the area around the pipe is refined in our simulations. This local refinement is needed to accurately resolve the deformed topography with less computational cost than using a global refinement for the entire domain. The finite volume method employs 182 non-uniform control volumes reconstructed from the finite element nodes located on the interface.

In Fig. 15 we display the responses of the water free-surface at six different instants namely, $t=0s$, $t=0.1\,s$, $t=1s$, $t=2s$, $t=3s$, $t=10s$ using open flow boundary conditions at both downstream and upstream. As can be seen from these results, the system starts

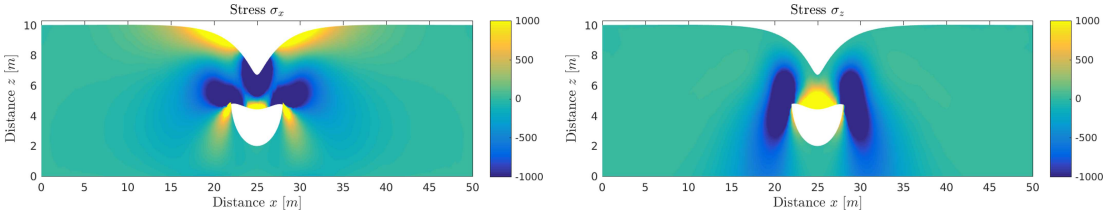

Figure 16: Distribution for the stresses σ_x (left) and σ_z (right) obtained for shallow water waves generated by pipe failure in the topography at $t=3s$.

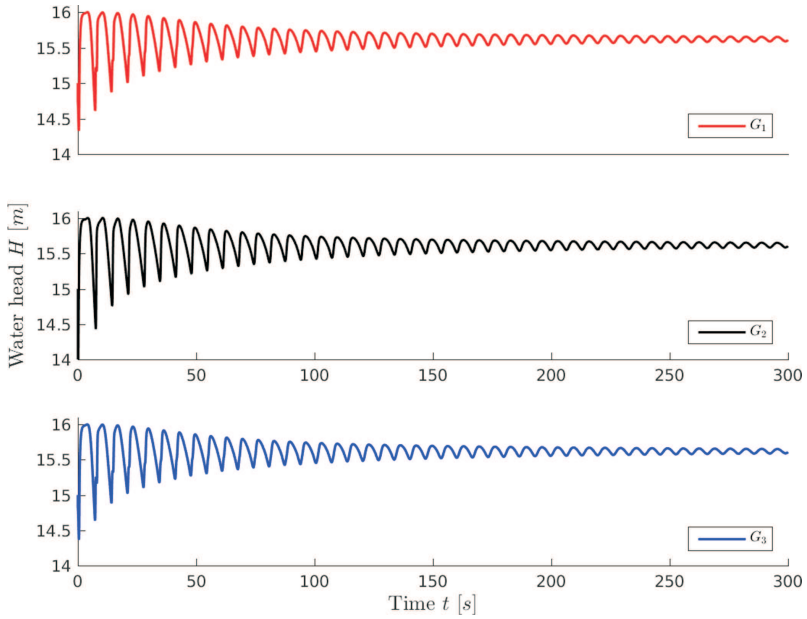

Figure 17: Time evolution of the total water head at the three gauges G_1, G_2 and G_3 obtained for shallow water waves generated by pipe failure in the topography.

from the rest and once the deformation on the pipe occurs, a water wave is generated on the free-surface and it flows over the deformed bed. For longer times, the system is stabilized to a steady-state configuration with no disturbances on the water free-surface. For the considered force on the pipe, the bed topography experiences a maximum vertical displacement of 3.25 m downwards. It is clear that the considered coupled finite element/finite volume method performs well for this free-surface flow problem over a deformable bed as both the bed topography and the water free-surface are accurately captured without non-physical oscillations or excessive numerical diffusion appearing in the numerical solutions.

Fig. 16 depicts distributions of the computed stresses σ_x and σ_z at time $t=3s$. Again, high stresses appear at the upper part of the pipe where the bed deformation is taken place. The results also illustrate localized stresses σ_x on the bed topography for this ex-

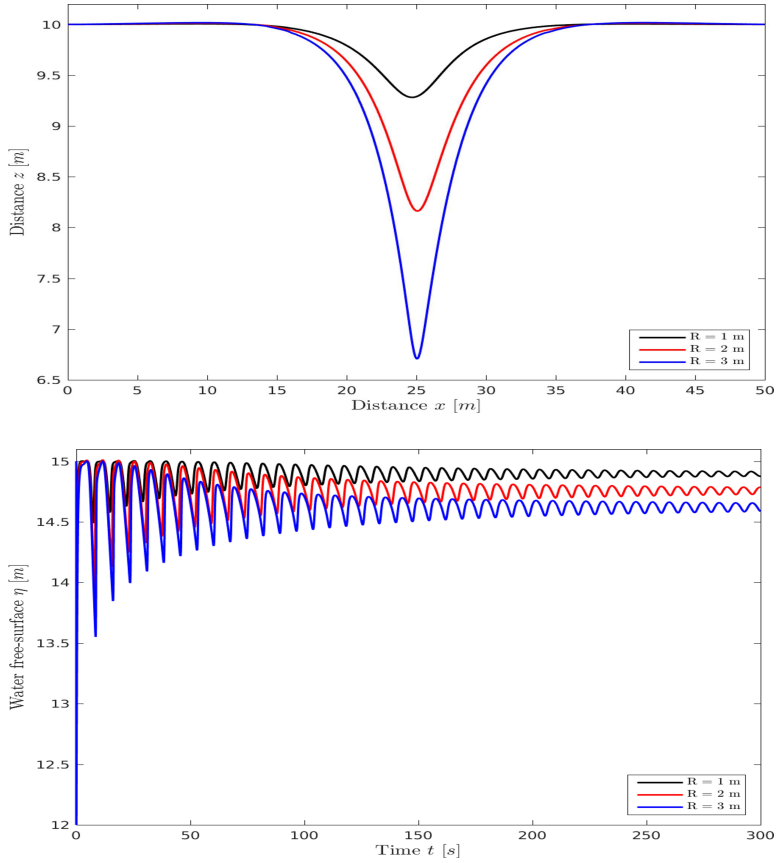

Figure 18: Bed deformation (top) time evolution of the free-surface at the gauge G_2 (bottom) obtained for shallow water waves generated by pipe failure in the topography using different values of the pipe radius.

ample. The perfect symmetry in the distribution of both stresses σ_x and σ_z should also be noted in Fig. 16. Next we consider reflective boundary conditions and in Fig. 17 we display the total water head at three gauges G_1, G_2 and G_3 selected at $x=22\,m$, $x=25\,m$, $x=28\,m$, respectively. It can be clearly shown from this figure that the waves at three considered gauges exhibit similar amplitudes and frequencies. On the other hand, because of the symmetry in the location, the wave features at the gauges G_1 and G_3 are almost the same.

Our next concern with this test example is to examine the impact of pipe size on the bed deformation and the free-surface waves. Here, we run the simulations using three pipes with radius $R=1\,m$, $2\,m$ and $3\,m$ keeping all the other parameters fixed as in the previous run. Fig. 18 shows the bed deformation and the time evolution of the free-surface at the gauge G_2 obtained for the considered values of the pipe radius. Table 4 summarizes the maximum values of the stress σ_z, the stress σ_x, the bed B, the free-surface η and the hydrostatic pressure p obtained for this run. It is evident that larger deformations in the

Table 4: Computational results for shallow water waves generated by pipe failure in the topography using different values of the pipe radius.

Radius (m)	$\max\sigma_z$ (KPa)	$\max\sigma_x$ (KPa)	$\max B$ (m)	$\max\eta$ (m)	$\max p$ (KN/m^2)
1	8.973	16.65	0.7178	16.7295	65.9574
2	3.3655	10.816	1.8370	17.8588	76.9677
3	2.2391	11.633	3.2926	19.2992	91.0519

bed topography are obtained for pipes with larger radius and consequently waves with higher amplitudes on the free-surface, compare the values of $\max B$ and $\max\eta$ in Table 4. The presented results demonstrate that the proposed computational model is suited for the prediction of shallow water waves by elastic deformations in the topography. It should be stressed that results from the proposed model should be compared to experimental measurements. However, there is no data available until now to carry out this work. Thus, at the moment we can only perform simulations and verify that results are plausible and consistent.

5 Conclusions

A simple and accurate computational model is proposed to simulate shallow water waves induced by elastic deformations in the bed topography. The mathematical model consists on coupling the nonlinear one-dimensional shallow water equations to the linear two-dimensional equations for elasticity. The coupling conditions between the two sets of equations are achieved through the interface between the water flow and the bed topography. The hydrostatic pressure and friction forces calculated from the water flow are applied as external forces on the interface for the elasticity model whereas, bathymetric forces are accounted for in the shallow water equations. As numerical solvers we considered a well-balanced finite volume method for the free-surface flow using non-uniform meshes and a robust finite element method for the bed deformation using unstructured meshes. The approach combines the attractive attributes of the finite volume discretization and the finite element method to yield a procedure for either flat or non-flat topography. Numerical results are presented for several test examples on shallow water waves induced by sudden changes in the bed topography. The results make it promising to be applicable also to real situations where, beyond the many sources of complexity, there is a more severe demand for accuracy in predicting free-surface waves induced by sudden bed deformations, which must be performed for long time. Finally, the models presented in this study do not account for the dispersion of surface waves during their long-time propagation. However, using ideas developed in [14, 15], it is possible to extend the proposed model to take into account these dispersion features in shallow water waves induced by elastic deformations in the bed topography.

References

[1] A. Abdollahi and H. Mason. Tsunami-induced pore water pressure response of unsaturated soil beds: Numerical formulation and experiments. *Computers and Geotechnics*, 110:19–27, 2019.

[2] S. Aiabadi, M. Akhbar, and R. Patel. Hybrid finite element/volume method for shallow water eqution. *International Journal for numerical methods in Engineering*, 83:1719–1738, 2010.

[3] C. Arvanitis and A. Delis. Behavior of finite volume schemes for hyperbolic conservation laws on adaptive redistributed spatial grids. *SIAM journal on scientific computing*, 28:1927–1956, 2006.

[4] F. Benkhaldoun, S. Sari, and M. Seaid. A flux-limiter method for dam-break flows over erodible sediment beds. *Applied Mathematical Modelling*, 36(10):4847–4861, 2012.

[5] P. Dellar. Non-hydrodynamic modes and a priori construction of shallow water lattice Boltzmann equations. *Phys. Rev. Estate. Nonlin. Soft Matters Phys*, 65:1–12, 2002.

[6] D. Dutykh and F. Dias. Tsunami generation by dynamic displacement of sea bed due to dip-slip faulting. *Mathematics and Computers in Simulation*, 80:837–848, 2009.

[7] C. Escalante, T. Luna, and M. Castro. Non-hydrostatic pressure shallow flows: GPU implementation using finite volume and finite difference scheme. *International Journal for Computer-aided Engineering and Software*, 338:631–659, 2018.

[8] U. Fjordholm and S. Mishra. Vorticity preserving finite volume scheme for the shallow water equations. *SIAM J. Sci. Comput*, 33:588–611, 2011.

[9] D. Fuhrman and P. Madsen. Tsunami generation, propagation, and run-up with a high oder Boussinesq model. *Coastal Engineering*, 56:747–758, 2009.

[10] F. Gao, D. Jeng, and H. Sekiguchi. Numerical study on the interaction between non-linear wave, buried pipeline and non-homogeneous porous seabed. *Computers and Geotechnics*, 30:535–547, 2003.

[11] S. Grilli and P. Guyenne. A fully non-linear model for three-dimensional overturning waves over an arbitrary bottom. *J. Fluid Mech*, 35:829–867, 2001.

[12] K. Kajiura. Tsunami source, energy and the directivity of wave radiation. *Bull. Earthquake Research Institute*, 48:835–869, 1970.

[13] N. Kato. Seismic cycle on a strike-slip fault with rate-and state-dependent strength in an elastic layer overlying a viscoelastic half-space. *Earth planets space*, 54:1077–1083, 2002.

[14] G. Khakimzyanov, D. Dutykh, Z. Fedotova, and D. Mitsotakis. Dispersive shallow water wave modelling. Part I: Model derivation on a globally flat space. *Communications in Computational Physics*, 23:1–29, 2018.

[15] G. Khakimzyanov, D. Dutykh, O. Gusev, and N. Shokina. Dispersive shallow water wave modelling. Part II: Ii: INumerical simulation on a globally flat space. *Communications in Computational Physics*, 23:30–92, 2018.

[16] X. Li and H. Castaneda. Damage evolution of coasted steel pipe under cathodic-protection in soil. *Anti-Corrosion methods and materials*, 64:118–126, 2017.

[17] P. Madsen, H. Bingham, and H. Liu. A new Boussinesq method for fully nonlinear waves from shallow to deep water. *J. Fluid Mech*, 462:1–30, 2002.

[18] R. Nicolaides. A method for complex geometries in finite-difference solutions of Maxwell's equations. *An international computers and mathematics with applications*, 48:1111–1119, 2004.

[19] J. Noorzaei, M. Viladkar, and P. Godbole. Nonlinear soil-structure interaction in plane frames. *Engineering computations*, 11:303–316, 1994.

[20] T. Ohmachi, H. Tsukiyama, and H. Matsumoto. Simulation of Tsunami induced by dynamic

displacement of seabed due to seismic faulting. *Bull. Seism. Soc. Am.*, 91:1898–1909, 2001.
[21] Y. Okumura and Y. Kawata. Effects of rise time and rupture velocity on Tsunami. In *Proceedings of the Seventeenth Internationsl Offshore and Polar Engineering Conference*, pages 2–20, July 2007.
[22] H. Poulos and E. Davis. *Elastic solutions for soil and rock mechanics*. The University of Sydney, Australia, 1991.
[23] B. Reddy and M. Kussner. Some low-order quadrilateral elements based on novel integration rules. *Engineering computations*, 15:700–720, 1998.
[24] N. Renon, P. Montmitonnet, and P. Laborde. Numerical formulation for solving soil/tool interaction problem involving large deformation. *Engineering computations*, 22:87–109, 2005.
[25] P. Roe. Approximate Riemann solvers, parameter vectors, and different schemes. *Journal of computational physics*, 43:357–372, 1981.
[26] R. Salmon. The lattice Boltzmann solutions of the three-dimensional planetary geostrophic equations. *J. Mar. Res*, 57:847–884, 1999.
[27] J. Stoker. *Water waves*. Interscience Publishers, Inc, New York, 1986.
[28] G. Strang. On the construction and the comparison of difference schemes. *SIAM J. Numer. Anal.*, 5:506–517, 1968.
[29] S. Thomas. A finite element model for the analysis of wave induced stresses, displacements and pore pressures in an unsaturated seabed i: theory. *Computers and Geotechnics*, 8:1–38, 1989.
[30] Y. Thorimbert, J. Latt, and B. Chopard. Coupling of lattice Boltzmann shallow water model with lattice-Boltzmann free-surface model. *Journal of computational science*, 33:1–10, 2019.
[31] M. Todorovska and M. Trifunac. Generation of Tsunamis by a slowly spreading uplift of the sea floor. *Soil Dynamics and Earthquake Engineering*, 21:151–167, 2001.
[32] E. Toro. *Shock-capturing methods for free-surface shallow flows*. Wiley and Sons, 2001.
[33] D. Wang, B. Bienen, M. Nazem, Y. Tian, J. Zheng, T. Pucker, and M. Randolph. Large deformation finite element analysis in geotechnical engineering. *Computers and Geotechnics*, 65:104–114, 2015.
[34] S. Wang. An improved high order finite difference method for non-conforming grid interfaces for the wave equation. *J Sci Comput*, 77:775–792, 2018.
[35] J. Zhang, J. Zhou, S. Bi, Q. Li, and Y. Fan. A well-balanced numerical scheme for shallow water simulation on adaptive grids. *Journal of physics*, 495:1–10, 2014.
[36] Q. Zhu, A. Cao, W. Zaifend, J. Song, and C. Shengli. Damage evolution of coasted steel pipe under cathodic-protection in soil. *Anti-Corrosion methods and materials*, 58:234–237, 2011.